Journal of Applied Fluid Mechanics, Vol. 17, No. 3, pp. 672-683, 2024.
Available online at www.jafmonline.net, ISSN 1735-3572, EISSN 1735-3645.
https://doi.org/10.47176/jafm.17.3.2105

Evaluation of the Cavitation Fluid Characteristics of the Bullet across the Medium into the Water at Different Velocities

Y. Liu [1, †], L. Wang [2], X. Peng [3], Y. Gu [3], Z. Zhou [3], P. Liu [1]and L. Huang [4]

[1] *School of Instrument Science and Engineering, Southeast University , Nanjing , Jiangsu Province,, 210000, China*
[2]*PipeChina, Guangzhou, Guandong Province, 510000, China*
[3] *Ministry of Education Key Laboratory of Testing Technology for Manufacturing Process, Southwest University of Science and Technology, Mianyang, Sichuan Province, 621010, China*
[4]*Yalong River Hydropower Development Company, Ltd., Chengdu, Sichuan Province, 610000, China*

[†] *Corresponding Author Email: 230228958@seu.edu.cn*

ABSTRACT

This paper studies the evolution and fluid distribution characteristics of a high-speed projectile's cavity in the water based on joint research, a method involving experiment and numerical simulation. Specifically, we develop an experimental platform and a numerical calculation model for a high-speed projectile to observe its initial cavity evolution characteristics in the water at different velocities and close ranges. Additionally, this work investigates the evolution mechanism of the cavitation process and its fluid distribution law inside the cavity and studies the evolution characteristics of the cavitation stage under different velocities. The results reveal that after the projectile enters the water, the cavity is gourd-shaped and symmetrical, with a necking phenomenon at the tail and the cavity falling off. The cavitation process can be divided into the surface closure, saturation, deep closure, and collapse stages according to the fluid distribution changes in the cavity. Suppose the projectile has a certain speed with the water, its velocity increases. In that case, the cavity generation rate decreases, the growth rate of the water vapor volume in the cavity decreases, the peak water vapor volume content reduces, and the volume of air in the saturation phase of the cavity becomes increases having a range of 6% to 9%. Additionally, the cavity surface closure dimensionless time grows logarithmically as the velocity changes from 0 m/s to 500 m/s, the cavity saturation dimensionless time decreases approximately linearly, and the cavity depth closure dimensionless time is unaffected by velocity changes.

Article History

Received June 21, 2023
Revised October 22, 2023
Accepted October 24, 2023
Available online January 1, 2024

***Keywords*:**

Cavity
Velocity
Fluid distribution characteristics
Projectiles
Numerical simulation

1. INTRODUCTION

When a projectile enters the water at high speed, the water in the local low-pressure region of its surface vaporizes and forms a cavity with other gases, such as air, called the cavitation phenomenon (Truscott & Techet 2009). Cavitation is a unique fluid-solid coupling phenomenon that is widely used in the research of underwater weapons drag reduction technology (Shi & Takami 2001; Bergmann et al., 2009; Tassin & Korobkin 2014; Panciroli et al., 2018; Treichler & Kiger 2020; Shokri & Akbarzadeh 2022; Janati & Azimi 2023).

Currently, most studies focus on the impact of the complex environment and the composite structure on the characteristics of the cavity (Worthington & Cole 1900; Lee et al., 1997; Wang et al., 2020a, b; Li et al., 2022; Liu et al., 2023). For instance, Zou et al. (2022) conducted experiments using a vehicle with gas jet entry and explored the effects of different jet volumes and water entry angles on cavity morphology and jet length. Yu et al. (2022) conducted numerical simulations of the super cavity vehicle's water entry and obtained the vehicle cavity's evolution, size, load, and pressure variation laws. Ma et al. (2014) experimentally studied the water entry process of spheres at different velocities to obtain the developmental evolution of spherical water entry cavities. They analyzed the effects of water entry velocity and surface wetting state on the evolution of the spherical

NOMENCLATURE

D_0	AUV diameter	$R_2(x)$	equation of shape of the model tail
L	AUV overall length	σ	cavity number
L_1	length of model head	α_v	vapor phase volume fraction
L_2	length of model middle	ρ_v	vapor density
L_3	length of model tail	ρ_1	liquid-phase density
$R_1(x)$	equation of shape of the model head	ρ	mixing density
p	mixed-phase pressure intensity	p_v	vapor phase pressure
u_i	speed of each phase	F_{vap}	empirical constant
F_{cond}	empirical constant	a_{nuc}	no volume fraction of condensable gases
R_B	radius of a gas nucleus	V_1	saturated volume of vapor in the cavity
V_2	saturated volume of air	V_C	maximum volume of the cavity
C	percentage of air volume	t_1	vacuolar surface closure stage
t_2	vacuolar growth link	t_3	vacuolar depth closure stage
Δt_1	vacuolar saturation stage	k	turbulent kinetic energy
ε	turbulent dissipation rate	G_k	turbulent kinetic energy generation term due to mean velocity gradient
G_b	buoyancy-induced turbulent energy generation term	Y_M	effect of pulsating expansion of compressible turbulence on total dissipation rate
σ_k	Prandtl number of k，1.0	σ_ε	Prandtl number of ε，1.2

water entry cavity. Zhao et al. (2016) investigated oblique water entry with different head types of projectiles using high-speed camera technology. They found that the cavity the projectile is attached to during the high-speed oblique water entry, and the cavity is symmetrical and unaffected by gravity. Besides, Song & Duan (2020) conducted water injection emission experiments on three types of projectile noses and lengths and analyzed typical pressure distributions. They concluded that the shape of the nose mainly affects the drag coefficient. Shi & Xiao (2022) analyzed the effects of warhead shape, launch speed, and surface wettability on cavity evolution and motion characteristics using warheads at different speeds and angles as experimental objects. In addition to the above research, we compared many other studies on projectile entry into water (Duez et al. 2007; May 2018).

In summary, the evolution mechanism of the cavitation phase and the classification criteria of a projectile's cavitation evolution is critical when studying the projectile's cross-media flight. Especially when coupled with the influence of the projectile's entry angle into the water, the evolution mechanism of the cavitation phase is more complex, and current research on this issue is very limited. Therefore, this paper takes the Mrying-type projectile model as the research object and establishes the multiphase flow calculation model for a high-speed projectile entering water across media. Our study considers the natural cavitation effect, introduces a 6-DoF algorithm and the dynamic grid technology, and obtains the calculation results of the projectile entering water navigation under different velocities. Additionally, we study and analyze the changing trend of different vapor and air quantities in the cavity, summarize the basis for dividing the different super-cavitation stages, and reveal the general influence of velocity on different stages of super-cavitation. This work provides an accurate process definition description method to study cavitation evolution.

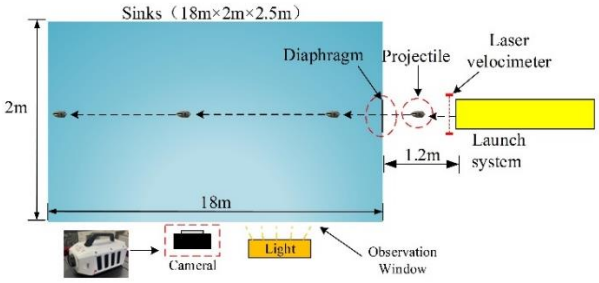

Fig. 1 Projectile's water entry test

2. EXPERIMENTAL PLATFORM CONSTRUCTION

Figure 1 illustrates the subsonic large-size projectile horizontal water entry experimental platform designed and built to facilitate the investigation in this paper. The experimental platform comprises four parts: a launching system, a water tank, a high-speed imaging system, and a protection device. The launch system shoots the projectile horizontally into the water tank, and the velocity measurement device measures the projectile's velocity into the water at the exit of the launch system. The high-speed imaging system captures the motion and cavitation evolution of the projectile underwater located beside the water tank.

The projectile launch system mainly comprises an attitude adjustment mechanism and a launch barrel. The launch system adopts a one-stage pneumatic launch setup, which provides flight kinetic energy for the projectile by releasing high-pressure gas reaching up to 20MPa.

The overall size of the flume is 18m (L) × 2m (W) × 2.5m (H), and an observation window with a diameter of D=0.5m is installed on one side of the flume to obtain a clear picture of the evolution of the projectile's underwater cavitation.

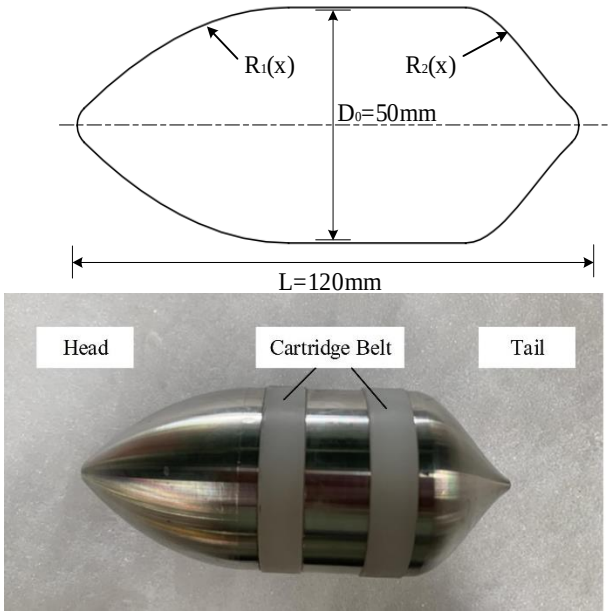

Fig. 2 Experiment projectile

The high-speed imaging system mainly comprises a high-speed camera, a light source, and a computer. The camera sampling resolution is set to 1280×720, the sampling frame rate is set to 10000 fps/s, the exposure time is adjusted to the maximum of 99μs, the gain value is the default, and the camera shooting time is adjusted to the maximum of about 5.36s. The camera is placed at a vertical distance of about 1.2m from the wall of the water tank, and the first optical observation window is used to shoot. According to the measurement, the projectile's flying distance was 0.66m.

The experimental projectile is designed based on the Mrying type of AUV structure (Li & Wang 2017). The diameter of model D_0 is 50mm, the overall length L is 120mm, and the cartridge's head, middle, and tail lengths are L_1=50mm, L_2=40mm, and L_3=30mm, respectively. The model is bolted together in three sections, and two annular nylon pouches are installed in the middle of the model during assembly to prevent the inner wall of the model from being worn when fired. The mass of the cartridge is 1.07kg, the material is 316L stainless steel, and the density is ρ=7.89g/cm3, as depicted in Fig. 2. The projectile's head shape is described by equation $R_1(x)$, and the tail shape by equation $R_2(x)$.

3. EXPERIMENTAL RESULTS AND ANALYSIS DISCUSSION

The experiments were conducted with the launch pressure as the input condition, and four experiments were conducted under the parameters reported in Table 1.

Figure 3 illustrates the evolution of cavitation after the projectile enters the water with a velocity of v=252.9617m/s using a launch pressure of 7MPa. At t=0ms, the camera captured the projectile. The experimental phenomena highlight that cavitation occurred immediately after the high-speed projectile

Table 1 Experiment data in the table

No.	Launch Pressure (Mpa)	Launch Velocity (m/s)	Launch Angle (°)
1	5	222.4265	0
2	7	252.9617	0
3	10	285.1531	0
4	15	327.0270	0

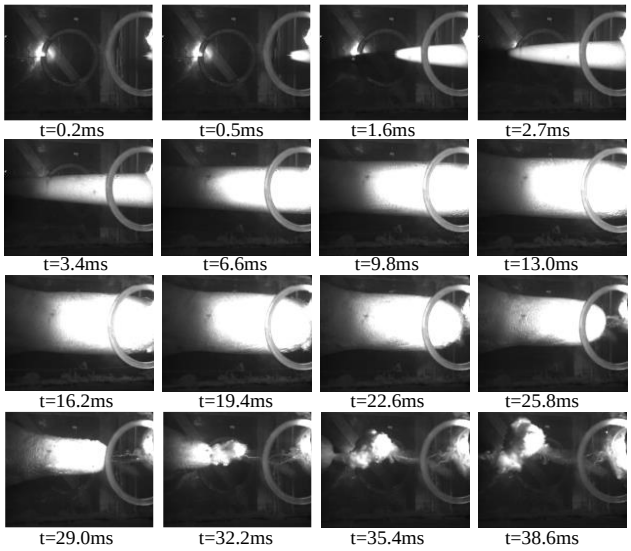

Fig. 3 Evolution of cavitation of the cartridge into the water at 7MPa

entered the water. The cavity was generated at the warhead, evolved from the shoulder to the side and rear, and then rapidly developed from local cavitation to super-cavitation, and the cavity was gourd-shaped as a whole. As the flight speed of the projectile decreases, the cavity size first increases and then decreases, followed by the closure of the cavity and accompanied by the phenomenon of necking of the tail. Finally, the cloud-like cavity group was discharged from the tail.

Given that the projectile entered the water with a velocity of v=252.9617m/s, the cavitation evolution process of the projectile entering the water with a subsonic velocity v=222.4265m/s, v=252.9617m/s, v=285.1531m/s, v=327.0270m/s was studied experimentally. Figure 4 presents the cavitation evolution process of the projectile at different entry velocities, which reveals that the cavitation of the high-speed projectile occurred immediately after entering the water.

The cavity was generated at the projectile's nose, evolving from the shoulder to the side and rear of the projectile, and the overall cavity developed from local cavitation to super-cavitation. The super cavity was gourd-shaped at the first cavity closure, followed by the necking phenomenon at the tail of the cavity. Finally, the cloud-like cavity cluster was discharged from the tail.

By comparing and analyzing the underwater cavitation process of the projectile at four different velocities, conclude the following: 1) The overall symmetrical

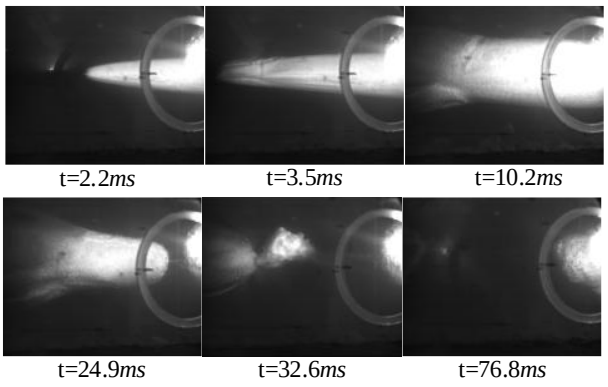

(a) v_1=222.4265*m/s*

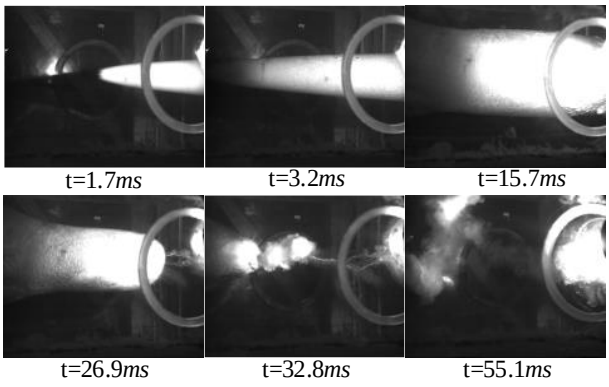

(b) v_2=252.9617 *m/s*

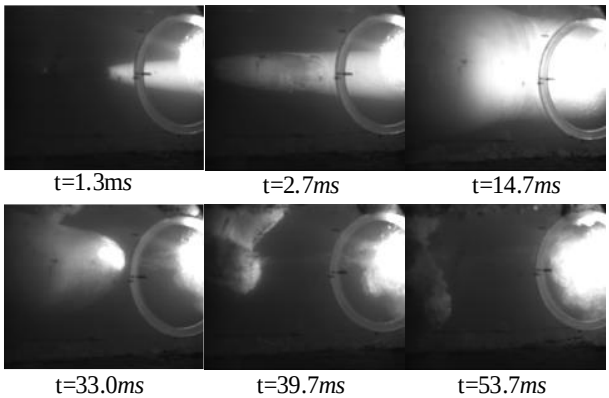

(c) v_3=285.1531*m/s*

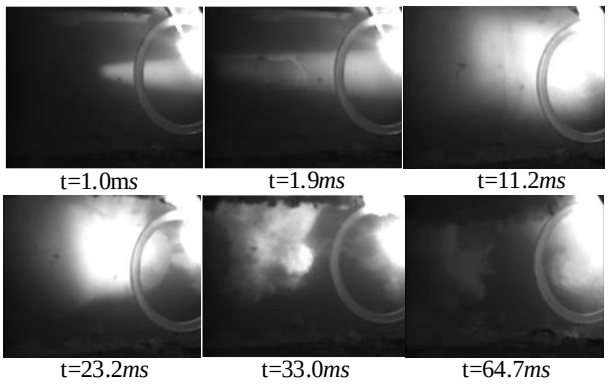

(d) v_4=327.0270*m/s*

Fig. 4 Evolution of the cavitation of the projectile into the water at different velocity

distribution of the attached cavity and the obvious necking phenomenon at the tail. 2) The attached cavity evolves significantly from the shoulder of the projectile and extends to the side and rear. 3) Many cloudy cavity clusters are discharged after the necking phenomenon occurs at the tail of the cavity. 4) The wall of the attached cavity is filled with many cloudy cavities, non-transparent walls and thus is unstable. 5) The projectile does not undergo obvious deflection in the navigation attitude. Since the velocity direction of the projectile is the same as the flight direction when it is launched, and the angle of attack is 0°, it will not form a head-on and back-flow surface after entering the water resulting in a different speed of cavity development. Cavitation non-constancy leads to uneven distribution of the wetted area of the projectile head, leading to uneven load direction on the head causing "tail beat motion". However, the angle of attack caused by the small range and short period will not have a large impact on the cavitation and, thus, on its overall symmetric distribution.

Additionally, due to the structural characteristics of the Mrying projectile, its head plays the role of cavitation during the voyage, so the cavity will first form a cavitation film covering the rear end of the warhead when the front end is generated. This happens until the film extends to the shoulder of the projectile and when the structure undergoes an obvious change in curvature. The cavity starts to extend to the side and rear to develop a super-cavitation state, with an overall gourd shape, as depicted in Fig. 5(a), which is the reason for the obvious cavity evolution from the shoulder of the elastic body observed in the experiment.

The experimental phenomenon also reveals that the non-transparent cavity wall has many cloud-like cavities. This phenomenon indicates a small-scale cavity cluster shedding phenomenon during cavity evolution and a significant cavity wall thickness. Unlike flat-headed, cone-headed, and other cartridges, the Mrying cartridge is more stable in the cavity flow field when navigating in the water, and there is no obvious vortex structure near the shoulder.

As the cavitation number decreases, a transparent film region and a vapor mixing pulsation region form at the head of the projectile. Besides, the frequent perturbation of the cavity clusters in the mixing region will lead to the random high-frequency shedding phenomenon and instability of the cavity wall during the cavity evolution, as illustrated in Fig. 5(b).

The reasons mentioned above lead to small-scale cavity cluster shedding, and the Mrying elastomer cavity cluster shedding belongs to natural shedding. The pressure inside the super cavity is less than the external water pressure. While the cavity is in all contact with water, the cavity in the wall will be re-liquefied and dissolved in water due to the external water pressure, and the internal cavity will continuously be consumed under the dual role of the necking phenomenon. At this time, the cavity's tail, due to the reverse jet caused by the reverse jet vortex, will separate the attached cavity and the tail cavity. Hence, for the tail discharge of the cloud-like cavity group, the experiments observed a composition of the vapor-gas mixture, shedding the tail cloud cavity quickly, followed by a local low-pressure area at the water inlet. The outside

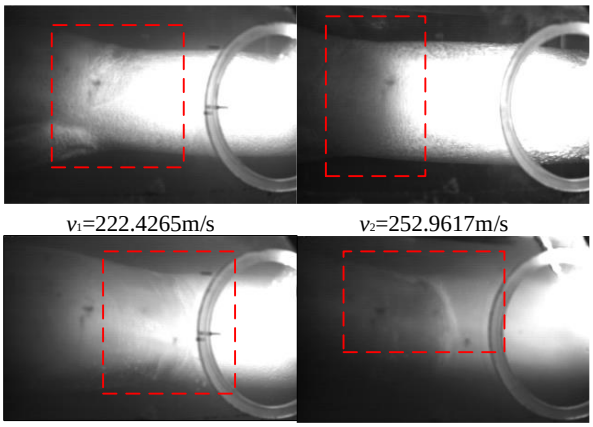

（a）Gourd-shaped cavity

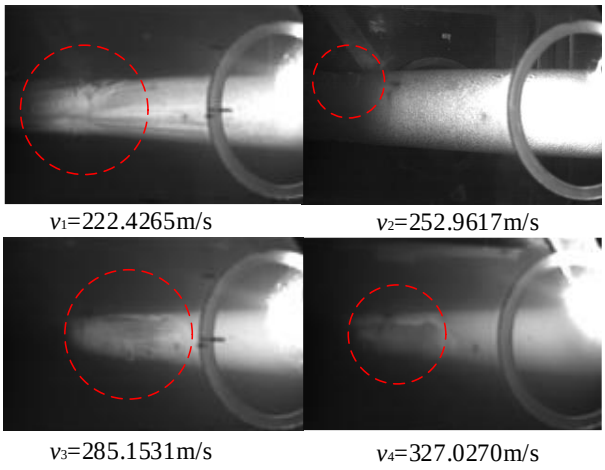

（b）Cavity wall disturbance

Fig. 5 Experimental Cavity Phenomena

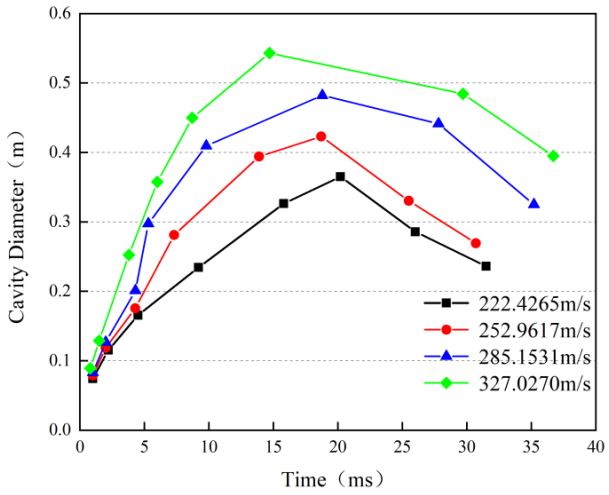

(a) Cavity Diameter

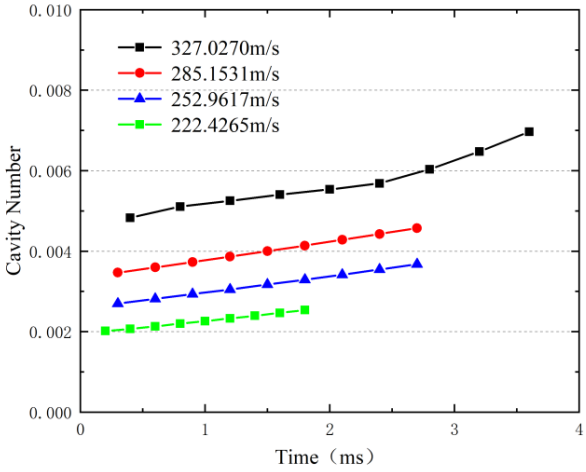

(b) Change in cavitation number

Fig. 6 Experimental cavitation properties

air into the water becomes a water-vapor mixture of air masses, and the higher stability of the air masses is annihilated slowly.

The deflection of the navigational attitude of the projectile mainly depends on its force. In the super-cavitation state, the force area of the projectile is divided into two parts: the wetted area of the warhead and the area inside the cavity. The wetted area is mainly affected by the incoming flow resistance, and the uneven force on the head due to the uneven wetted area causes the tail beat motion of the projectile. However, its tail beat range is small, and the short period and other characteristics will not make the projectile attitude deflect strongly. The cavity can be regarded as an isobaric zone, and the force inside the cavity is uniform. Additionally, the warhead does not form a head-on or back-flow surface, and the cavity development progress is the same and symmetrically distributed, which will not form a local pressure differential on the projectile's body.

In addition to the common points mentioned above, different water entry velocities have obvious effects on the evolution of cavitation: 1) The cavity size is different. The larger the water entry velocity, the larger the maximum diameter of the cavity and the longer the maximum length. 2) The necking phenomenon is different. The larger the water entry velocity, the weaker the necking, and the later the tail cavity is shed. Figure 5 infers that at the early stage of cavity development, there is no big difference in the diameter of the cavity under different water entry speeds. The difference becomes more obvious with the continuous development of the cavity. Figure 6 presents the curve of cavity size under different water entry speeds. Figure 6 (a) suggests that the cavity's maximum diameter increases with the water entry velocity increase. In addition, the larger the water entry velocity, the earlier the maximum diameter of the cavity appears and the slower the cavity collapse rate. In this experiment, the minimum diameter of the cavity is 0.365m at the entry velocity v=222.4265m/s, and the maximum diameter of the cavity is 0.541m at the entry velocity v=327.0270m/s. Besides, Fig. 6 (b) reveals that the larger the projectile's velocity, the smaller the cavitation number, the larger the radius of the vacuole, and the wider the vacuole coverage area, which is consistent with the current research theory. In this experiment, the cavitation number of the Mrying projectile with v=327.0270 m/s is minimum σ=0.00202.

In summary, several shortcomings exist in the experimental study of the cavitation fluid properties of high-speed projectiles across media. Therefore, further investigation is required in combination with numerical simulation methods.

4. NUMERICAL CALCULATION METHOD

This paper uses the volume of fluid (VOF) multiphase flow model in the numerical simulation to describe the multiphase flow formed by gas, vapor, and liquid. We assume that the fluid is incompressible, and we ignore the thermal effect due to fluid viscosity during the water entry process.

After comparing and selecting cavitation models, it was found that the Zwart-Gerber-Belamri cavitation model can cause non physical phenomena in the calculation process. Therefore, we chose the Schnerr-Sauer model. The Schnerr-Sauer cavitation model is used for the solution of the cavitation problem (Schneer & Sauer, 2001), where the vapor phase volume fraction satisfies the following equation:

$$\frac{\partial \alpha_v}{\partial t}+\frac{\partial\left(\alpha_v u_i\right)}{\partial x_i}=F_{vap}\frac{2\alpha_{nuc}\left(1-\alpha_v\right)\rho_v}{R_B}\sqrt{\frac{2}{3}\frac{p_v-p}{\rho_l}}-F_{cond}\frac{2\alpha_v\rho_v}{R_B}\sqrt{\frac{2}{3}\frac{p-p_v}{\rho_l}} \tag{1}$$

The Realizable $k-\varepsilon$ turbulence model is used for the turbulence model, this turbulence model assumes that the water flow is incompressible and does not consider the thermal effect caused by fluid viscosity during the calculation process, which is defined as follows (Yu et al., 2022):

$$\frac{\partial}{\partial t}(\rho k)+\frac{\partial}{\partial x_j}\left(\rho k u_j\right)=\frac{\partial}{\partial x_j}\left[\left(\mu+\frac{\mu_t}{\sigma_k}\right)\frac{\partial k}{\partial x_j}\right]+G_k+G_b-\rho\varepsilon-Y_M+S_k \tag{2}$$

$$\frac{\partial}{\partial t}(\rho\varepsilon)+\frac{\partial}{\partial x_j}\left(\rho\varepsilon u_j\right)=\frac{\partial}{\partial x_j}\left[\left(\mu+\frac{\mu_t}{\sigma_k}\right)\frac{\partial\varepsilon}{\partial x_j}\right]+\rho C_1 S\varepsilon-\rho C_2\frac{\varepsilon^2}{k+\sqrt{v\varepsilon}}+C_{1\varepsilon}\frac{\varepsilon}{k}C_{3\varepsilon}G_b+S_\varepsilon \tag{3}$$

The water domain size is 18m×2m×2.5m, and the air domain size is 0.5m×2m×2.5m. The rest of the boundary conditions are consistent with the experimental environment, and the calculation domain is presented in Fig. 7.

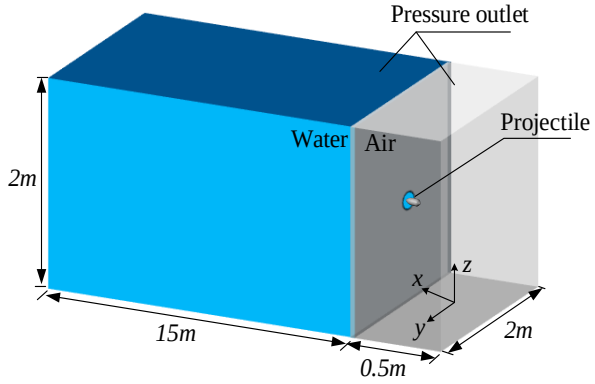

Fig.7 Sketch of the computational domain

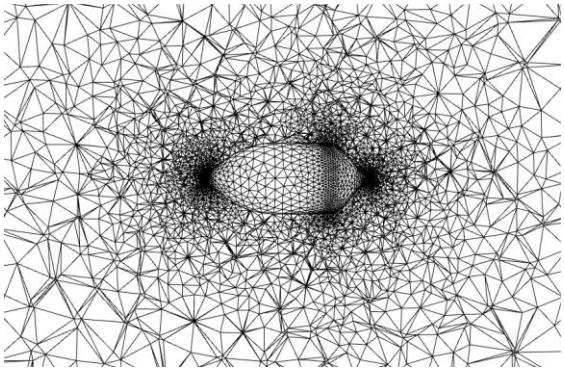

Fig. 8 Sketch of the computational domain for mesh

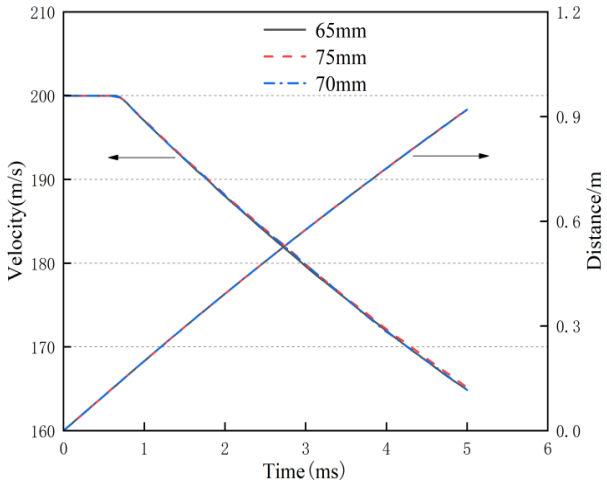

Fig. 9 Variation of projectile velocity and travel distance with time for different grid sizes

For the overall calculation domain, a tetrahedral unstructured grid with a cell size of 70 mm is used, and to improve the calculation accuracy of the multiphase coupled flow field, the mesh of the contact interface of the projectile is encrypted with a size of 5 mm. The total number of grid cells is 715783 (see Fig. 8), which is combined with the 6-DoF algorithm to realize the corresponding motion calculation of the projectile model.

The grid size independence was verified for a water entry velocity of v=200m/s. The grid cell sizes were 65mm, 70mm, and 75mm, and the total number of grids was 861892, 715783, and 575015. Figure 9 presents the velocity and depth variation curves when the projectile enters water under different grid sizes. The velocity and depth of the projectile entering the water with time are the same for different grid sizes. Hence, a cell size of 70mm was chosen for calculation while considering calculation efficiency. In addition, a comparison and selection of time steps, turbulence models, and cavitation models were also conducted, and the following calculation parameters were ultimately determined: time step t=10^{-5}s, Realizable k-epsilon turbulence model, and Schnerr Sauer cavitation model. The other parameters adopt typical literature settings, such as Volume Fraction of 0.5, Turbulent Kinetic of 0.8, and Turbulent dispersion of 0.8. The pressure velocity coupling scheme is SIMPLE, and in the

spatial differentiation method, the pressure and momentum are second-order upwind, while the rest are first-order upwind. The distinct format of the time term is first-order implicit (Ma et al., 2014; Wang et al., 2020b; Yu et al., 2022; Zou et al., 2022).

The accuracy of the numerical algorithm was verified for the projectile entry across the medium while using the constructed experimental platform. The projectile velocities were tested and numerically simulated at 222m/s, 252m/s, and 285m/s, respectively, and the average velocities of the 7 flight segments at 0.8ms intervals within 0.66m range after water entry were compared with the simulation results. Figure 10(a) illustrates the corresponding results inferring that compared with the experimental test results, the mean deviations of the simulated entry velocities of 222m/s, 252m/s, and 285m/s are 0.36%, 0.52%, and 0.86%, respectively. Thus, the simulated results greatly agree with the experimental test results.

The experimental results are highly consistent with the simulation results by comparing the cavitation evolution of the projectile in water (see Fig. 10(b)). Therefore, the established calculation model of the projectile entering the water at different velocities is accurate.

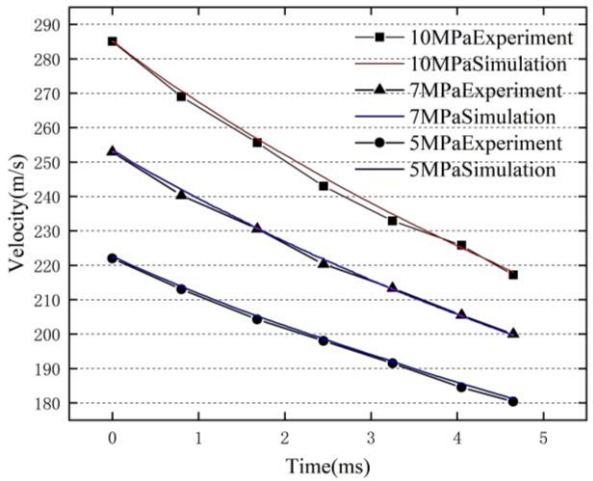

(a) Different speed comparison.

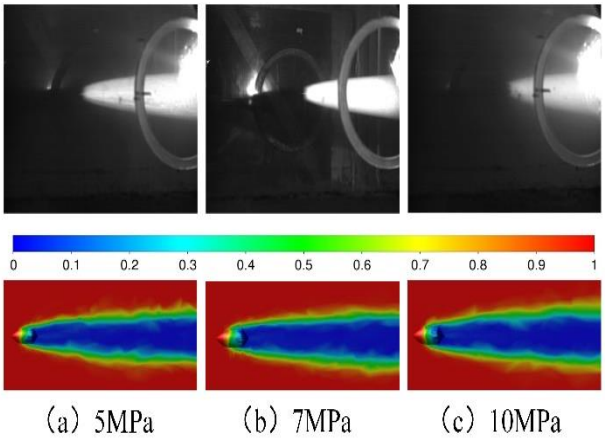

(b) Cavity comparison.

Fig. 10 Comparison of simulated and experimental results

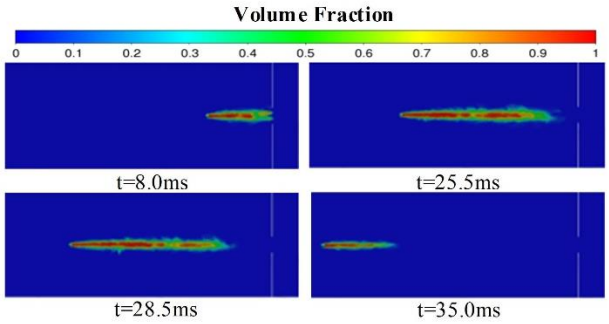

(a) Water vapor phase volume distribution cloud map

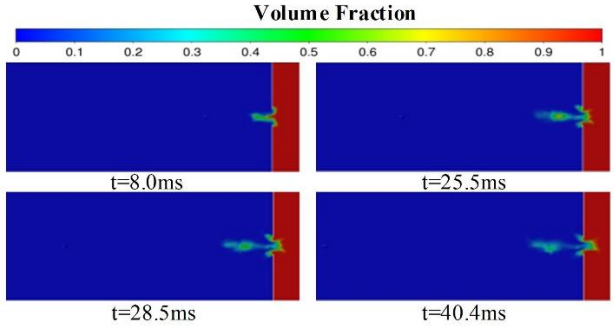

(b) Air phase volume distribution cloud map

Fig. 11 Contour of volume fractions of vapor and air

5. NUMERICAL CALCULATION RESULTS AND ANALYSIS DISCUSSION

The development of cavities in the cavitation process was characterized by distinct phases through experimental phenomena. Under the influence of multiphase flow coupling, the fluid distribution inside the cavity of the underwater projectile changes continuously, and the cavitation process exhibits multiple phase changes under the effect of cavity fluid evolution with time. Figure 11 presents the cloud diagram of the two-phase volume distribution of water vapor and air for the Myring projectile model entering the water at an angle φ=0° and a velocity of 200 m/s.

Under the influence of the local low-pressure region, the cavitation phenomenon occurs immediately after the projectile enters the water and develops from local cavitation to a super-cavitation state within a short time. In the process of cavitation development, the volume of water vapor inside the cavity continuously increases and occupies the main part of the cavity, while the air outside the water tank rushes into the tail of the cavity and forms the cavity together with water vapor. Subsequently, the cavity completed surface and deep closure, and the water vapor and air inside the cavity were separated. Thus, the fluid distribution inside the cavity significantly changed.

The evolutionary stages of the cavitation process can be divided according to the change in the fluid distribution inside the cavity. The water vapor and air inside the cavity and the air in the water tank can be quantified and analyzed, as shown in Fig. 12.

During the evolution of cavitation, the water vapor volume in the cavity increases and then decreases due to

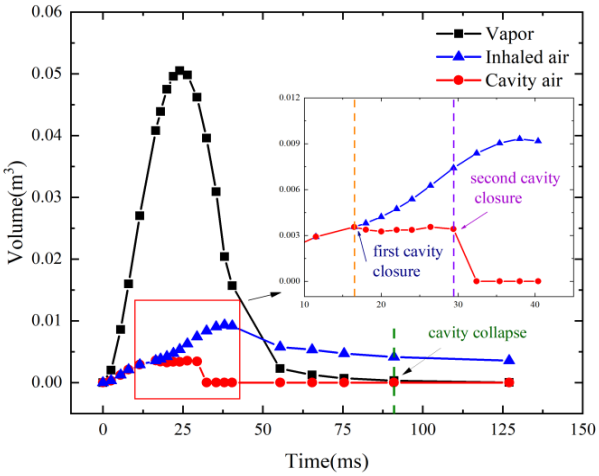

Fig. 12 Variation of the volume of vapor, cavity air, and inhaled air with time

the decreasing velocity of the projectile. It reaches a peak at *t*=24ms. The cavitation process can be divided into cavity growth and dissipation links based on the volume change trend of water vapor. The air volume in the cavity shows an increase in saturation and a sudden drop in the changing trend. The air in the cavity and the air in the water tank at the beginning of the volume change are the same, but at *t*=16.5ms, when the cavity completed surface closure, they changed the separation trend as the cavity air moved into the saturation stage. For *t*=29.4ms, the cavity completed depth closure, the cavity water vapor and air separation, and the fluid in the cavity containing only water vapor remained. According to the changing trend of air volume in the cavity, the cavitation process can be further divided into four stages: cavity surface closure stage, cavity saturation stage, cavity depth closure stage, and cavity collapse stage.

Based on the analysis of the projectile entering the water at *v*=200m/s, we study the fluid distribution characteristics in the cavity at *v*=100m/s, *v*=200m/s, *v*=300m/s, *v*=400m/s, and *v*=500m/s. The volume distribution of the water phase of the projectile entering the water at different velocities is depicted in Fig. 13, where Fig. (f) shows a local zoom in for v = 200 m/s, further demonstrating the details of the multi-phase flow inside and close to the of the cavity. As the velocity increases, the overall curvature of the cavity appearance increases, the difference in the duration of each stage of the cavitation increases, and the fluid distribution within the cavity develops continuously. As the velocity increases from *v*=100m/s to *v*=500m/s, the closure time of the cavity surface gradually extends.

Under the influence of velocity, the projectile cavity exhibits non-constant development characteristics, and the fluid distribution inside the cavity produces significant changes, as shown in Fig. 14 (a) to 13(b).

Figure 14(a) reveals that as the velocity of the projectile into the water increases, the peak volume of water vapor in the air bubble of the projectile is larger and appears earlier, with the maximum volume being 0.274 m^3, and the minimum volume being 0.0341 m^3. Figure 14(b) highlights that as the velocity of the projectile into the water increases, the peak air volume in the projectile's air bubble is larger, appears earlier, and lasts longer. Combined with Figs. 14 (a) and Figs. 14 (b), we obtain the variation law of the cavitation phase time with the projectile's velocity into the water. Specifically, as the projectile's velocity into the water increases, the air bubble surface closure phase time increases, the air bubble saturation phase time remains unchanged, the air bubble depth closure phase time increases, and the air bubble collapse time increases. The specific average values for different velocities underwater are reported in Table 2, where V_1 is the saturated volume of water vapor in the cavity, V_2 is the saturated air volume, V_c is the maximum volume of the cavity, and C is the percentage of air volume.

Table 2 Fluid volume parameters inside the cavity in the table

v(m/s)	V_1(m^3)	V_2(m^3)	V_c(m^3)	*C*
100	0.0404	0.00235	0.04275	5.50%
200	0.0505	0.00336	0.05386	6.24%
300	0.1300	0.00565	0.13565	4.17%
400	0.2490	0.01530	0.26430	5.79%
500	0.2840	0.01750	0.30150	5.80%

Table 2 infers that as the velocity of the projectile into the water gradually increases from 100m/s to 500m/s, the air volume ratio in the air bubble increases then decreases, and finally increases. When the velocity of the projectile into the water is within 100m/s to 200m/s, the proportion of air volume gradually increases. When the velocity of the projectile further increases towards the critical point of the sound speed, the air volume proportion gradually decreases. Additionally, when the projectile's velocity exceeds the critical point to reach supersonic speed, the proportion of air volume in the air bubble gradually increases with the increase of the water velocity. When the velocity exceeds 400m/s, the proportion of air volume tends to stabilize.

In order to further investigate the general influence of the projectile's velocity degree in the water on the evolutionary stage of cavitation (Hu et al., 2018), the dimensionless times were obtained from processing the data in Fig. 14. The corresponding results are reported in Table 3, where t_1 is the vacuolar surface closure stage, t_2 is the vacuolar growth link, t_3 is the vacuolar depth closure stage, Δt_1 is the vacuolar saturation stage. The formula for calculating dimensionless time is:

$$t_d = t \times \sqrt{g / R} \tag{4}$$

Where g is gravitational acceleration, R is projectile radius, t_d is dimensionless time.

Table 3 Dimensionless time in the table

v(m/s)	t_1	t_2	t_3	Δt_1
100	0.236	0.343	0.463	0.225
200	0.275	0.475	0.641	0.366
300	0.326	0.530	0.833	0.518
400	0.388	0.605	0.986	0.597
500	0.437	0.635	1.049	0.611

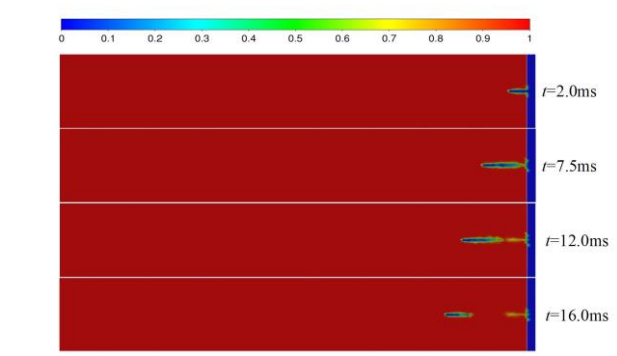

(a) v=100m/s

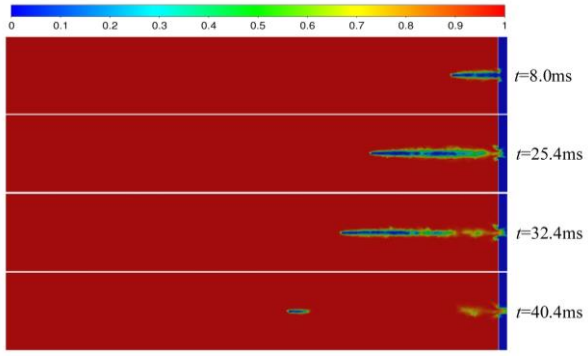

(b) v=200m/s

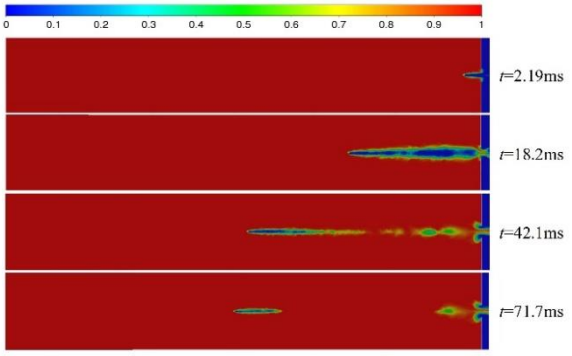

(c) v=300m/s

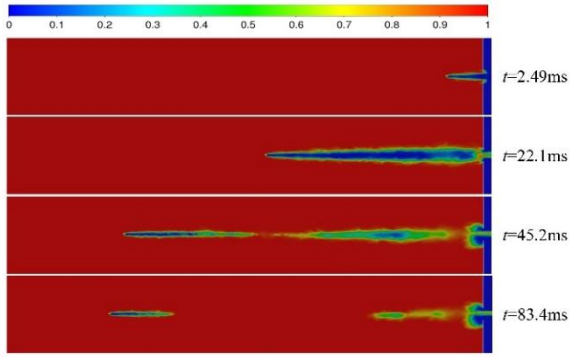

(d) v=400m/s

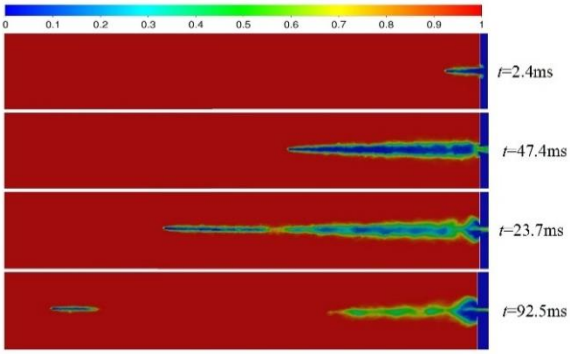

(e) v=500m/s

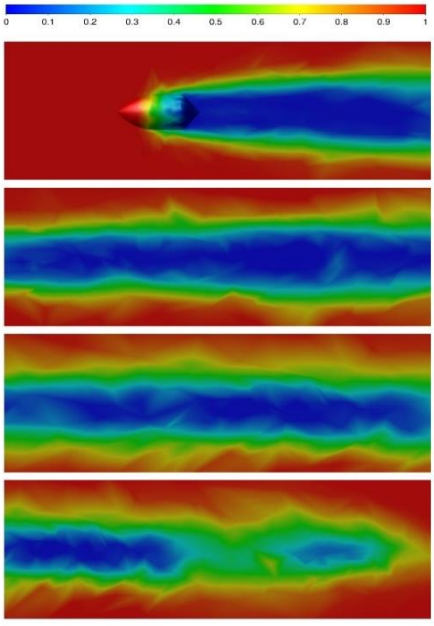

t=25ms

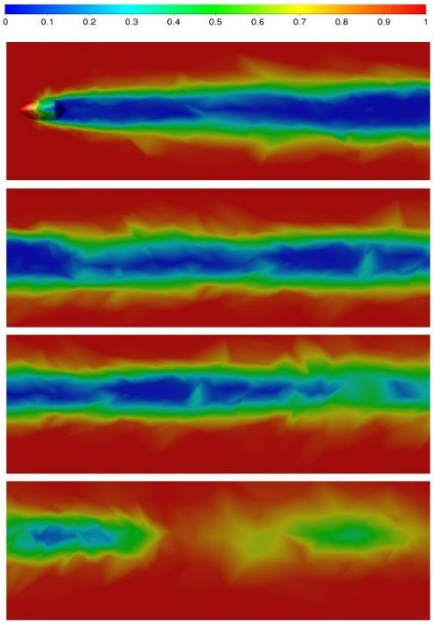

t=30ms

（f）Cavitation Enlargement

Fig. 13 Contour of volume fractions of water at a different velocity of entry of the projectile

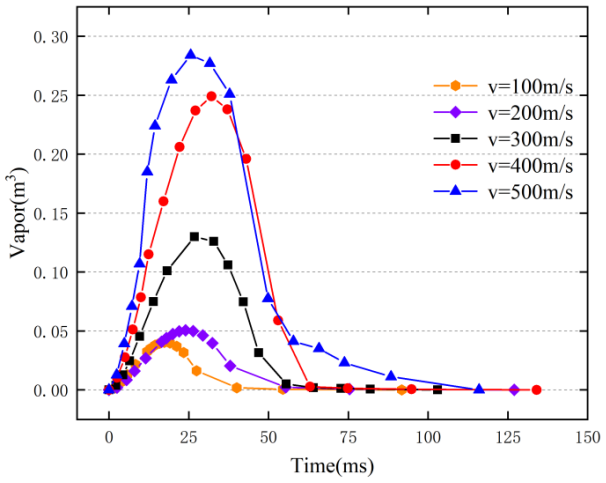

(a) vapor

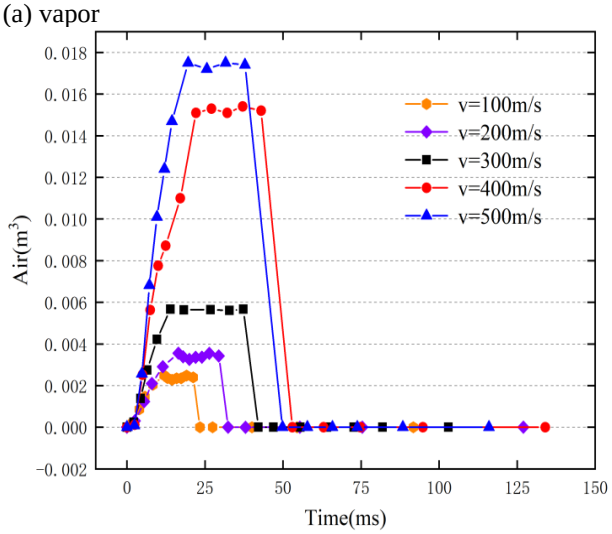

(b) air

Fig. 14 Variation of the volume of vapor and air inside the cavity with time

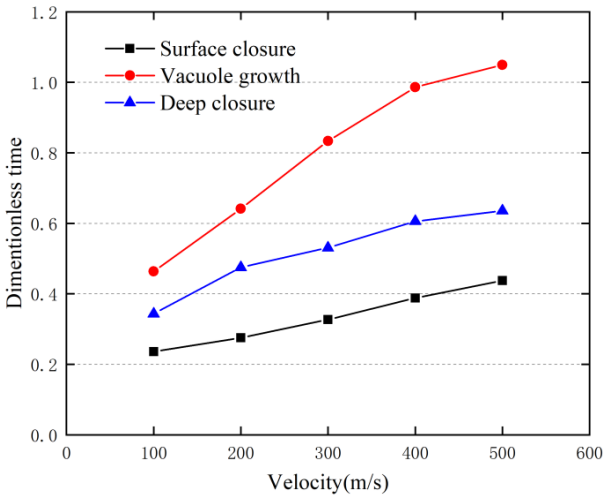

(a)Variation of dimensionless time of cavity with deg

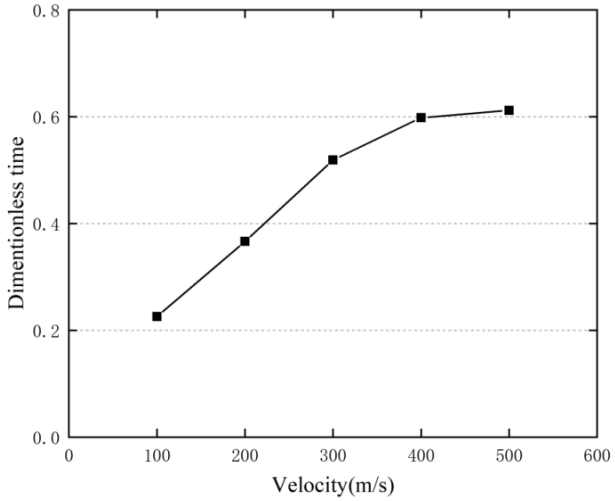

(b)Variation of dimensionless time of cavity saturationstage with deg

Fig. 15 Variation of dimensionless time

By observing Table 3, it can be found that the dimensionless time of each stage in the evolution of cavitation changes significantly with the change of the velocity of the projectile into the water, as shown in Fig. 15. With the gradual increase of the projectile water entry velocity from 100m/s to 500m/s, the dimensionless times of the surface closure phase, growth link, depth closure phase and saturation phase of the vacuole are all growing, but they are slightly different in the growth situation. The surface closure phase of the vacuole and the depth closure phase are similar, both of them are closer to the linear growth trend; the growth phase of the vacuole and the saturation phase are similar, with a linear growth until the velocity of the projectile reaches 400m/s, after which the growth rate slows down and eventually plateaus.

6. CONCLUSIONS

This article combines experimental and numerical simulation research methods to establish an experimental platform and numerical calculation model for high-speed projectiles entering water. The evolution characteristics of the initial cavity of the projectile towards the water at different speeds were observed at close range, and the evolution mechanism of the cavitation process, fluid distribution law, and evolution characteristics of the cavitation stage in the cavity at different speeds were studied. The conclusions of this work are as follows:

(1) In the experiment, cavitation occurred immediately after the projectile entered the water and developed from local cavitation to super-cavitation. The vacuole was generated in the evolution of the warhead to the side and rear, and there was an obvious necking phenomenon at the tail of the vacuole. A large number of cloud-like bubbles were discharged, the overall symmetric distribution was gourd-shaped, the vacuole had the phenomenon of vacuole group shedding and wall disturbance, and there was no obvious deflection of the attitude during the navigation of the projectile.

(2) Based on the Realizable k-ε model and the Scherr-Sauer cavitation model, the cavitation evolution and characteristics of the projectile entering the water with different velocities are studied in the simulation. During the evolution of cavitation, the fluid distribution characteristics inside the cavity change significantly, and the cavitation process can be divided into cavity growth and cavity dissipation according to the law of water vapor volume change. According to the trend of air volume

change inside the cavity, the cavity evolution process can be clearly defined into four stages: the surface closure stage, saturation stage, deep closure stage, and collapse stage.

(3) The projectile's velocity into the water will affect the shape of the vacuole, the internal fluid, each cavitation stage, and other vacuolar fluid properties. As the velocity of the projectile increases, the larger the peak volume of water vapor inside the projectile vacuole, the larger the peak volume of air inside the projectile vacuole, the earlier it appears, the longer it lasts, the faster the growth rate of the length of the projectile vacuole, and the maximum vacuole length become larger. The maximum diameter of the projectile vacuole gradually increases, but its increase rate does not change significantly.

(4) The fluid-structure coupling and fluid dynamics characteristics of high-speed projectiles entering water through media are extremely complex, and research using numerical simulation will be limited by computational resources, and the cost of using experiments will be high. Therefore, the research content and depth of this article are limited. Most current research results focus on the cavitation research of simple structured projectile bodies after entering the water. Whether the obtained research results and laws apply to complex structured projectile bodies entering the water. Further research on complex structured projectile bodies entering water is required to summarize the influence of their structural parameters on relevant fluid characteristics, such as the volume of the projectile cavity, the position of the multi-degree of freedom center of gravity, and structural parameters such as the tail wing.

ACKNOWLEDGEMENTS

This research was supported by the Post graduate Research and Practice Innovation Program of Jiangsu Province (No. SJCX21_0040).

CONFLICT OF INTEREST

The authors declare that they have no known competing financial interests or personal relationships that could have appeared to influence the work reported in this paper.

DATA AVAILABILITY

Data will be made available on request.

AUTHORS CONTRIBUTION

Youchen Liu: The numerical simulation calculations. **Libin Wang:** The high-speed projectile's water entry experiment. **Xiaowu Peng** and **Youkai Gu**: Data collection. **Pengfei Liu and Zhi Zhou**: Prepared all figures. **Liangxiong Huang:** Polish the paper.

REFERENCES

Bergmann, R., Van, D., Gekle, S., Van, A., & Lohse. D. (2009). Controlled impact of a disk on a water surface: Cavity dynamics. *Journal of Fluid Mechanics*, *633*, 381-409. https://doi.org/10.1017/S0022112009006983

Duez, C., Ybert, C., & Clanet, C. (2007). Making a splash with water repellency. *Nature Physics*, *3*(3), 180-183. https://doi.org/10.1038/nphys545

Hu, M. Y., Zhang, Z. H., Liu, J. B., & Meng, Q. C. (2018). Fluid-solid coupling numerical simulation on vertical water entry of projectile at low subsonic speed. *Acta Armamentaria*, *39* (03), 560-568. https://doi.org/10.3969/j.issn.1000-1093.2018.03.018

Janati, M., & Azimi, A. H. (2023). On the crown formation and cavity dynamics of free-falling thick disks. *Physics of Fluids*, *35* (1), 012104. https://doi.org/10.1063/5.0126864

Lee, M., Longoria, R. G., & Wilson, D. E. (1997). Cavity dynamics in high-speed water entry. *Physics of Fluids*, *9* (3), 540-550. https://doi.org/10.1063/1.869472

Li, Z. T., Zhao, S. P., Lu. B. J., & Yu, Y. (2022). Numerical simulation of multiphase flow field and trajectory characteristics of high－speed spinning projectile entry water in wave. *Journal of Vibration and Shock*, *41* (08), 55-71. https://doi.org/10.13465/j.cnki.jvs.2022.08.007

Li, Z., & Wang, Y. H. (2017). Autonomous underwater vehicle appearance and propulsion system optimization design, *Journal Of Machine Design*, *34* (05), 23-29. https://doi.org/10.13841/j.cnki.jxsj.2017.05.005

Liu, W. T., Zhang, A. M., Miao, X. H, Ming, F. R., & Liu, Y. L. (2023). Investigation of hydrodynamics of water impact and tail slamming of high-speed water entry with a novel immersed boundary method. *Journal of Fluid Mechanics*, *958*, A42. https://doi.org/10.1017/jfm.2023.120

Ma, Q. P., He, C. T., Wang, C. H., Wei, Y. J., Lu, Z. L., & Sun, J. (2014). Experimental investigation on vertical water-entry cavity of sphere. *Explosion And Shock Waves*, *34* (2), 174-180. https://doi.org/10.11883/1001-1455(2014)02-0174-07

May, A. (1951). Effect of surface condition of a sphere on its Water entry cavity . *Journal of Applied Physics*, *22*(10), 1219-1222. https://doi.org/10.1063/1.1699831

Panciroli, R., Pagliaroli, T., & Minak, G. (2018). On air-cavity formation during water entry of flexible wedges. *Journal of Marine Science and Engineering*, *6* (4), 155. https://doi.org/10.3390/jmse6040155

Schnerr, G. H., & Sauer, J. (2001). *Physical and numerical modeling of unsteady cavitation dynamics*. 4th International Conference on Multiphase FlowAt: New Orleans USA. https://www.researchgate.net/publication/296196752

Physical and Numerical Modeling of Unsteady Cavitation Dynamics

Shi, H. H., & Takami, T (2001). Some progress in the study of the water entry phenomenon. *Experiments in Fluid*, *30* (4), 475-477. https://doi.org/10.1007/s003480000213

Shi, Y., & Xiao, P. (2022). Experimental research on the influences of head shape and surface properties on the water entry cavity. *Journal of Marine Science and Engineering*, *10*(10), 1411. https://doi.org/10.3390/jmse10101411

Shokri, H., & Akbarzadeh, P. (2022). Experimental investigation of water entry of dimpled spheres. *Ocean Engineering*, *250*, 110992. https://doi.org/10.1016/j.oceaneng.2022.110992.

Song, Z. J., & Duan, W. Y. (2020). Experimental and numerical study of the water entry of projectiles at high oblique entry speed. *Ocean Engineering*, *211*, 107574. https://doi.org/10.1016/j.oceaneng.2020.107574

Tassin, A., & Korobkin, A. A. (2014). Cooker, M.J, On analytical models of vertical water entry of a symmetric body with separation and cavity initiation. *Applied Ocean Research*, *48*, 33-41. https://doi.org/10.1016/j.apor.2014.07.008

Treichler, D. M., & Kiger, K. T (2020). Shallow water entry of supercavitating darts. *Experiments in Fluids*, *61*, 1-17. https://doi.org/10.1007/s00348-019-2862-7

Truscott, T. T., & Techet, A. H (2009). Spin on cavity formation during water entry of hydrophobic and hydrophilic spheres. *Physics of Fluids*, *21* (12), 121703. https://doi.org/10.1063/1.3272264

Wang, R., Liu, C. L., Zhao, S. F., & Qi, X. B. (2020a). Numerical simulation for rotating motion of a natural super-cavitating vehicle. *Journal of Vibration and Shock*, *39* (21), 65-70. https://doi.org/10.13465/j.cnki.jvs.2020.21.009

Wang, W., Wang, C., Song, W. C., & Li, C. H. (2020b). Influence of sideslip angle on wetted area in turning motion of a supercavitating vehicle. *Journal of Vibration and Shock*, *39* (12), 135-141. https://doi.org/10.13465/j.cnki.jvs.2020.12.018

Worthington, A. M., & Cole, R. S. (1900). Impact with a liquid surface,studied by the aid of instantaneous photography. *Philosophical Transactions of the Royal Society a Mathematical Physical and Engineering Sciences*, *194* (252-261), 175-199. https://doi.org/10.1098/rsta.1900.0016

Yu, Y. L., Shi, Y., Pan, G., & Che, P. Q. (2022). Numerical analysis of cavitation and load characteristics of supercavitating vehicle entering water at high speed. *Journal of Northwestern Polytechnical University*, *40* (03), 584-591. https://doi.org/10.1051/jnwpu/20224030584

Zhao, C. G., Wang, C., Wei, Y. J., Zhang, X. S., & Sun, T. Z. (2016). Experimental study on oblique water entry of projectiles. *Modern Physics Letters B*, *30* (28), 1650348. https://doi.org/10.1142/S0217984916503486

Zou, Z. H., Li, J., Yang, M., Liu, H. S., & Jiang, Y. H. (2022). Experimental investigation on cavity flow characteristics of water entry of vehicle with gas jet cavitator. *Journal of Ballistics*, *34*, 1-8+97. https://doi.org/10.12115/j.issn.1004-499X(2022)01-001